

Shape from Scattering: Shape Estimation for Translucent Objects Based on Light Transport Analysis

CHIKA INOSHITA^{1,a)} YASUHIRO MUKAIGAWA² YASUYUKI MATSUSHITA¹ YASUSHI YAGI¹

Abstract: Accurate shape measurement has a long history in computer vision yet still remains a challenging task. In particular, a translucent object is one of the most difficult targets because of complex scattering and transmission of light in the media, which cannot be represented by a simple image formation model. To address this issue, we propose a *shape from scattering* framework, which enables estimation of 3D shape of translucent objects by either exploiting or explicitly modeling scattering. Our key idea is to represent the inherently complex relationship between the object shape and scene appearance due to scattering using a simple yet accurate model. Because the scattering distribution depends on optical properties of target material, we first measure and analyze a light transport on various types of translucent material as 8-dimensional bidirectional scattering surface reflectance distribution function (8D BSSRDF), then determine appropriate parameters of a scattering model. Based on the analysis of BSSRDF, we estimate object shape from observed appearances with a light attenuation model of single scattering for optically thin material and convolutional scattering distribution model for optically thick material, respectively. We show the effectiveness of our shape estimation method with experiments using translucent objects in real scenes. Although scattering has been regarded as a nuisance and eliminated by employing various pre-processing methods in the past, our *shape from scattering* framework eliminates the need of such external methods and makes direct inference of object shape in the presence of scattering.

1. Introduction

Shape measurement techniques are used in various industrial situations, such as visual inspection, digital archiving of world heritage and obtaining object models for computer graphics. Acquisition of object shapes broadens application of computer vision, thus, shape estimation methods have been advanced for various types of material such as metal [1], glass [2], [3], and water [4]. It is still challenging to obtain the shape of translucent objects, which transmits and scatters incident light in their subsurface because characteristics of illuminated light on their surface change from simple diffuse reflection. As pointed out by Godin *et al.* [5], the brightest observation of incident light on a translucent surface is shifted by scattering. Holroyd and Lawrence [6] also show the error in shape estimation with sinusoidal projection patterns for translucent objects depends on the degree of translucency of the target object. There are many translucent objects around us such as wax, marble, plastic products, and precious stones. Shape estimation for translucent objects remains an important and open problem.

While scattering is well studied in the field of computer graphics to render realistic images, it is less discussed in computer vision because complicated light interactions on the object surface generated by scattering render inverse problems difficult. Scattering has thus been regarded as a nuisance and eliminated by

various approaches in applications of computer vision such as polarization [7], coating with diffuse powder [8], high-frequency illumination [9], [10], analysis of the light field [11], and phase-shift method [12]. However, these methods need an additional preprocessing stage, and it remains difficult to completely ignore the effect of strong scattering [6]; *e.g.*, the phase-shift method requires modulation of the projection pattern depending on the degree of translucency of the target material [13]. Consequently, shape estimation without the reduction of scattering phenomena is required.

Contributions of the thesis

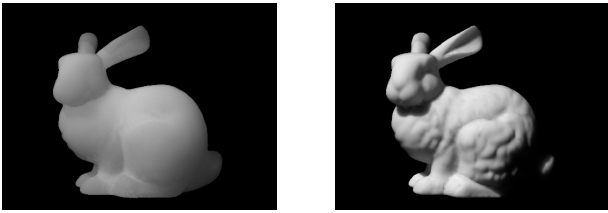
This thesis proposes a new shape estimation framework named *shape from scattering*, where the shape of a translucent object is estimated from the observed scattering itself. While the image formation model of translucent objects is needed to estimate the object shape from observed appearances, it is challenging because outgoing light from a point on the object surface is an integration of lights from neighboring areas. Thus, we need a simple image formation model for the shape estimation in practice. The image formation models substantially vary by optical property of target material as shown in Fig. 1. While shading in Fig. 1 (a) is greatly smoothed, that in (b) is only slightly smoothed. To deal with these differences of object appearance, we need to select an appropriate observation model for each material. Based on prior discussion, we develop a *shape from scattering* in the following steps.

(1) Measurement and analysis of light transport on a translu-

¹ Osaka University

² Nara Institute of Science and Technology

^{a)} inoshita@am.sanken.osaka-u.ac.jp



(a) Optically thin translucent object (b) Optically thick translucent object

Fig. 1 Examples of translucent appearance. Although the shape and illumination are the same, the observed translucent appearances differ in terms of the optical thickness.

cent surface: Because an observed appearance depends on a light transport on the object surface, we measure a light transport of various translucent materials and analyze their characteristics to select appropriate scattering models. To observe light transport on a surface, we use a polyhedral mirror to spherically distribute virtual cameras and projectors around target surface. We also analyze the sampled light transport to obtain a more simple representation of scattering light in translucent media by visualization and angular decomposition of light transport.

(2) Development of a shape estimation algorithm based on an appropriate scattering model: From the analyzed light transport, we develop image formation model for translucent objects in a simple but accurate expression. We construct an image formation model for optically thin translucent objects with single scattering, which is refractive light. We also construct a formation model for optically thick translucent objects with convolutional scattering model, which spatially distributes light. Based on these simple image formations, object shapes are estimated from observed intensities.

2. Related work

In this section, we summarize related work focusing on the measurement and analysis of light transport in scattering media and shape measurement under various light transport on object surfaces.

2.1 Measurement and analysis of light transport in scattering media

While scattering has been regarded as a nuisance, recent researches analyze complex scattering effect to obtain optical properties of target media.

Single scattering as a simple one-bounce scattering model is often used to estimate optical parameters of homogeneous media [14], [15] and spatial distribution of scattering media [16]. Of course, general scattering also has been analyzed by employing approximated scattering distributions. Jensen *et al.*'s dipole model is the representative multiple scattering model [17], and Mukaigawa *et al.* [18] estimated scattering parameters of plastics based on the dipole model. Gkioulekas *et al.* [19] analyzed the object appearance with a phase function, which controls shape of scattering distributions.

While a usual conventional camera observes target scenes with an exposure time in the unit of milliseconds, recent ultrafast camera can observe light propagations at trillion frames per second [20]. Because time-scale images represent a process of light

propagation, Wu *et al.* [21] identify the type of light interaction in a scene and estimate scattering parameter from images captured by ultrafast camera. Additionally, they extend normally four-dimensional light field into a five dimensional light field [22] with time-scale images. Although time-scale images are useful to analyze scattering light, we need an expensive ultrafast imaging system. We thus analyze the scattering light captured by a conventional camera and develop a shape estimation method based on the scattering characteristics.

2.2 Shape measurement for various light interactions

Shape-from-intensity

Shape-from-intensity is a generic framework for shape measurement from observed intensities. Traditional shape-from-intensity estimates the object shape from diffuse reflection [23], [24] or specular reflection [1], [25]. Recent methods focusing on other types of light interactions on an object surface are also used such as iridescence [26], attenuated light from light source [27] and multi-spectral polarization [28]. While object shapes can be directly estimated from local light interactions, the use of global light interactions such as interreflections and scattering is difficult because they do not directly relate to object shape.

Interreflection and scattering often increase the intensity of the unilluminated area with repeatedly reflected or propagated light rays on the target surface or in the subsurface. Thus, the surface shape is estimated from simulated interreflections [29] and light transport on target object [30]. However, scattering has not been used in the context of shape estimation because of the difficulty of exact rendering of scattering light.

Shape measurement of transparent objects

Transparent objects also transmit incident light in a similar manner to translucent objects. As light does not spread in a transparent object, shape of transparent objects is easily estimated from the path of the refracted light.

Most existing methods use pixel correspondence between the observed appearance and known background texture to obtain the light path in transparent media [4], [31]. However, it is difficult to estimate the original background from the appearance of transparent objects. Hence, the light is tracked with other types of light interactions, such as use of specular reflection and transmission [2], the light field probe [32], multiple interreflections in the object with polarization [3], partially reflected light [33] and phase imaging with coherent illumination [34].

Even though our target object is not a transparent object, refracted light is an informative cue in shape estimation. In fact, we estimate the shapes of optically thin translucent objects using refracted light in the target objects.

Shape measurement under scattering effects

Scattering has been removed in shape estimation by including an additional preprocessing stage. In contrast, underwater imaging techniques analyze target scenes in the presence of scattering because scattering light in underwater is simply attenuated in the medium. Narasimhan *et al.* [35] and Tsiotsios *et al.* [36] modeled attenuation of light propagation, and estimate reflectance of the target object. However, these methods cannot be directly applied to estimate the shape of translucent objects because incident

light spreads in translucent objects.

While shape estimation from scattering effects remains a challenging problem, Dong *et al.* [37] estimated the shapes of translucent objects from observed intensity that includes scattering effects. They represent complex scattering process in simple model under assumption of an optically thick homogeneous medium, and estimate object shape from observed appearances. Our proposal is similar to this approach, where we use a simple scattering model according to the analysis of light transport in translucent media.

3. Representation of light transport

Before beginning the main discussion, we describe the basic theory of light transport with emphasis on a translucent surface. We first present typical light transport phenomena on a translucent surface and then discuss the representation of light transport.

3.1 Light transport on a translucent surface

When a light ray strikes a translucent surface, the light partially is reflected on the surface, and partially transmits and scatters in the medium as shown in Fig. 2. The ratio of the surface reflection and subsurface scattering is physically determined by the Fresnel reflectance and transmittance [38]. Although distributions of reflected and scattered light are complicated, they can be simply categorized into several elementary components.

Surface reflection is categorized into two basic types: diffuse and specular reflections. Diffuse reflection reflects light in all directions from a microscopically rough surface. Ideal diffuse reflection is well known as Lambertian reflection [39]. Specular reflection reflects light to directions around the mirror reflection direction. Reflection gives an object a glossy or shiny appearance depending on the observation angle.

Subsurface scattering is also categorized into two types: Single and multiple scattering. This categorization depends on the number of collisions between light and particles in the medium. While single scattering is a single collision of light with a particle in the medium, multiple scattering is the collision of light with particles more than once in the medium before being observed. The light path of single scattering is determined by refraction on an object surface, because the single scattering changes the traveling direction of light only once in the medium. In contrast, the light path of multiple scattering cannot be identified because repeated scattering produces an uncountable number of light paths. As a result, the light of multiple scattering travels and distributes completely random in the media.

3.2 Representation of light transport

As described in Sec. 3.1, light transport can be characterized as outgoing distributions of light produced by varying incident light. This means that light transport can be represented by a relationship between the incident light ray and outgoing light ray. A *bidirectional scattering surface reflectance distribution function* (BSSRDF) provides a framework to express the light transport on an object surface [40] with the incident and outgoing light ray. Figure 3 illustrates the notion of the BSSRDF.

The BSSRDF represents the ratio of outgoing light from point

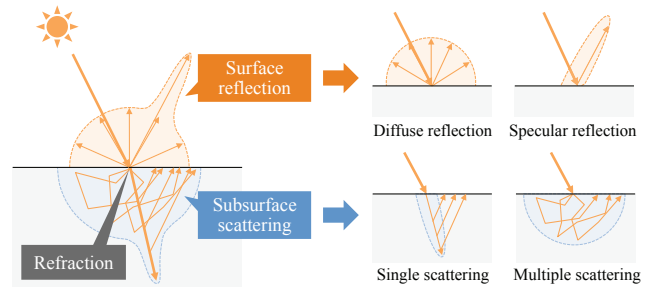


Fig. 2 Overview of light transport on a translucent surface. Incident light not only reflects on a surface but also travels into the medium. The direction of a light ray changes on a surface because of refraction.

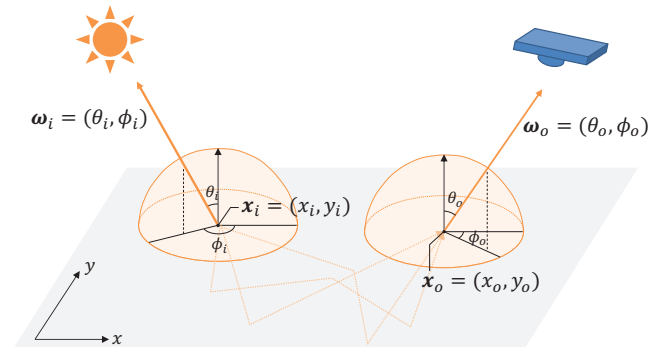


Fig. 3 Notion of the *bidirectional scattering surface reflectance distribution function* (BSSRDF). When a light ray coming from ω_i incidents at point x_i , part of the light scatters into the subsurface. After scattering in the medium, light outputs from a different point x_o and is distributed in the direction ω_o .

$x_o = (x_o, y_o)$ in direction $\omega_o = (\theta_o, \phi_o)$ to incident light at point $x_i = (x_i, y_i)$ from direction $\omega_i = (\theta_i, \phi_i)$, and is thus expressed

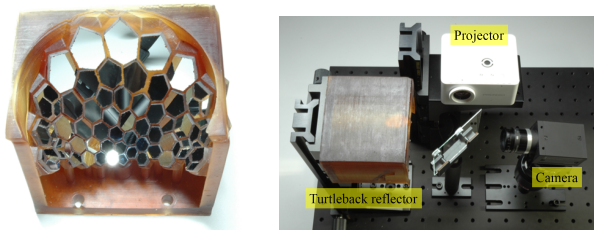
$$f_{BSSRDF}(x_i, \omega_i, x_o, \omega_o). \quad (1)$$

The BSSRDF is an eight dimensional function defined by four positional parameters and directional parameters.

4. Measurement and Analysis of Light Transport with Full-dimensional BSSRDF

To analyze light transport on translucent objects, we need to measure the full-dimensional BSSRDF that represents general light transport in real scenes. However, it has been challenging researchers have measured only low-dimensional BSSRDFs for the analysis of isotropic scattering or propagating light in optically homogeneous media [41]. Sampling of the full-dimensional BSSRDF is achieved by capturing the intensity for all possible illumination and observation directions via surrounding illumination and observation of the target medium. As this sampling takes an enormous time and requires large numbers of devices, an appropriate sampling method is needed for the measurement.

In this section, we present a sampling and analysis method for the full-dimensional BSSRDF. We use a polyhedral mirror system to place many virtual cameras and projectors around the target medium. We also analyze the sampled BSSRDF by visualizing four-dimensional slices and decomposing into them isotropic and anisotropic components to observe the characteristics of light transport. This analysis is the first attempt to sample and analyze a full-dimensional BSSRDF for general translucent objects.



(a) Turtleback reflector (b) System overview

Fig. 4 Turtleback Reflector [43]. The combination of the reflector with a camera and a projector. Many virtual cameras and projectors can be distributed on a hemisphere.

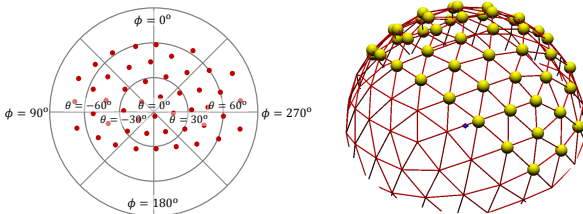


Fig. 5 Sampling positions on a hemisphere. Left: virtual cameras and projectors are placed uniformly in a spherical coordinate system. Right: sampling positions correspond to the vertexes of the geodesic dome.

4.1 Sampling the full-dimensional BSSRDF

To sample the BSSRDF, we need to surround the target object with many cameras and projectors. Obviously, such large numbers of devices are impractical. Therefore, mirror systems [42], [43] are often used to produce many virtual cameras and projectors. While existing mirror systems are designed for special imaging methods such as shallow depth-of-field imaging and confocal imaging, these systems can observe target scenes from various directions with controlled illuminations. We reuse the Turtleback reflector shown in Fig. 4, which is developed in previous research [43]. The sampling densities of the incident position \mathbf{x}_i and outgoing position \mathbf{x}_o are 20 by 20 and 100 by 100, respectively. The number of sampling directions of ω_i and ω_o is 48. Figure 5 shows the position of the virtual cameras and projectors. In total, 19,200 (48 incident directions \times 20 by 20 resolution) images are captured for BSSRDF sampling. If the shutter speed is set to 100ms, the total sampling time becomes 32 minutes. Although the sampling is sparse, the full-dimensional (eight-dimensional) BSSRDF can be obtained using our optical device.

We sampled BSSRDFs of three different materials, namely (a) epoxy resin, (b) rubber eraser, and (c) marble, as shown in Fig. 6. These materials have different properties of translucency. The epoxy resin is optically thin, while the rubber eraser is optically dense. The marble is a typical inhomogeneous material. Square regions indicated by red broken lines show the sampling areas. Figure 6 shows examples of images captured by virtual cameras that are enhanced by gamma correction ($\gamma = 2.0$). The left column of Fig. 6 shows images captured by different virtual cameras under the same incident light. These are four-dimensional (\mathbf{x}_o, ω_o) slices of the sampled BSSRDFs under fixed illumination $\mathbf{x}_i = (0, 0)$ and $\omega_i = (2.2^\circ, 154.3^\circ)$. Each small block shows the brightness at each outgoing position \mathbf{x}_o from a particular outgoing direction ω_o . The right column of Fig. 6 shows images captured by the same virtual camera under different incident lights. These

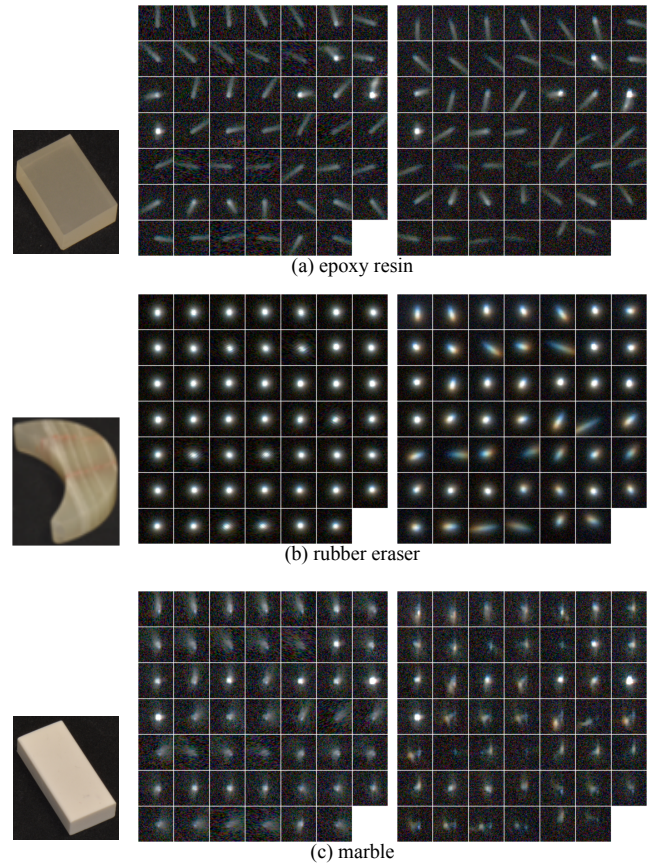


Fig. 6 Examples of images captured by virtual cameras. The left column shows images captured by different virtual cameras under the same incident light. The right column shows images captured by the same virtual camera under different incident lights. These images are enhanced by gamma correction ($\gamma = 2.0$).

are four-dimensional (\mathbf{x}_o, ω_o) slices sampled from the fixed incident point $\mathbf{x}_i = (0, 0)$ and outgoing direction $\omega_o = (2.2^\circ, 154.3^\circ)$. As there is color bleeding in the captured images owing to the color filter pattern of the projector, we analyze the scattering intensities in grayscale. Although simple analysis of the spatially distributed light with fixed illumination and observation directions is possible, it is difficult to observe the directionally distributed light for the outgoing direction from measurements in Fig. 6. Here, we analyze the sampled BSSRDFs in terms of both directional and spatial distribution.

4.2 Analysis of Sampled BSSRDF

In the first, we analyze sampled BSSRDFs by visualization. It is difficult to directly show the eight-dimensional function $f(\mathbf{x}_i, \omega_i, \mathbf{x}_o, \omega_o)$. Hence, we visualize the low-dimensional BSSRDF $f(\mathbf{x}_o, \omega_o)$ with fixed incident light.

Figure 7 shows four-dimensional slices $f(\mathbf{x}_o, \omega_o) = f(x_o, y_o, \theta_o, \phi_o)$ of the BSSRDF at a couple of incident positions as six-dimensional slices $f(\mathbf{x}_i, \mathbf{x}_o, \omega_o) = f(x_i, y_i, x_o, y_o, \theta_o, \phi_o)$ of the BSSRDF. The direction of illumination is fixed at $\omega_i = (44.9^\circ, 74.8^\circ)$. We plot the value of the BSSRDF at \mathbf{x}_o from -10 to 10 in 10 intervals for all viewing directions in log-scale pseudo color on a spherical coordinate system at each outgoing position. The center and right columns in Fig. 7 show four-dimensional slices of the BSSRDF obtained with illumination at

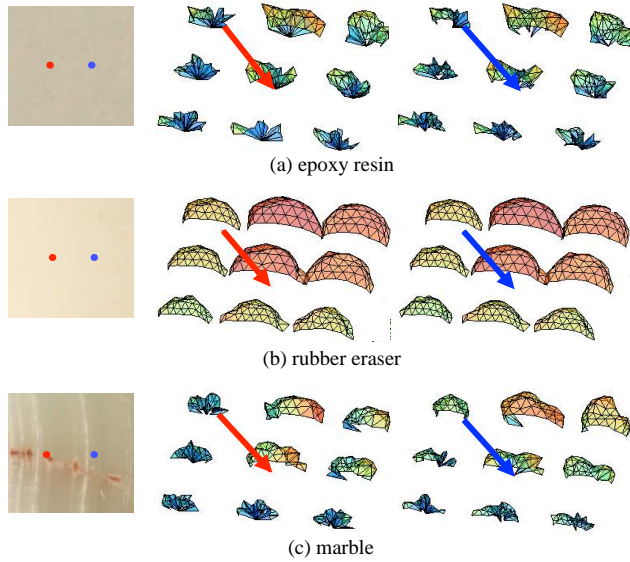


Fig. 7 Visualized BSSRDF. The direction of illumination is fixed at $(\theta_i, \phi_i) = (44.9^\circ, 74.8^\circ)$. The left column of images in (a) - (c) shows illuminated positions for the visualization of each material. The center column of images in (a) - (c) presents visualizations of the BSSRDF for illumination at the red point. The right column of images in (a) - (c) presents visualizations of the BSSRDF for fixed illumination at the blue point. The red arrow shows the direction of illumination.

the red and blue points, respectively. Figure 7 (a) shows slices of the BSSRDF of epoxy resin in which there is a straight light distribution. Visualized directional distributions at each position have a peak value for a specific direction and BSSRDFs have large values along the azimuth angle of the direction of illumination. This shows that scattering in epoxy resin is accounted for by single scattering because single scattering preserves the directionality of incident light. Additionally, slices of BSSRDFs are similar despite having different incident positions because epoxy resin is a homogeneous medium. Figure 7 (b) shows a visualized slice of the BSSRDF of rubber eraser. BSSRDF slices obtained for different incident points are also similar owing to the homogeneity. The directional distribution at each position has an almost constant value that decreases with distance from the incident point. This shows that multiple scattering loses the directionality of the incident light and is distributed uniformly among the outgoing directions. Figure 7 (c) shows the visualized BSSRDF of marble. Because marble is optically thin, light propagates in a particular spatial region as for epoxy resin. However, slices of BSSRDFs for different incident positions are not the same owing to the inhomogeneous structure. As eight-dimensional BSSRDF includes spatial information such as the incident and outgoing positions, we can analyze the spatial structure according to the similarity of BSSRDF slices.

Figure 8 shows six-dimensional slices $f(\omega_i, \mathbf{x}_o, \omega_o) = f(\theta_i, \phi_i, x_o, y_o, \theta_o, \phi_o)$ of the BSSRDF. The red distribution is obtained for the direction of illumination $(\theta_i, \phi_i) = (44.3^\circ, 127.2^\circ)$, and the blue distribution is obtained for $(\theta_i, \phi_i) = (43.7^\circ, 233.7^\circ)$. Directions of illumination are almost symmetric. Optically thin materials such as epoxy resin and marble changes the shape of the distribution according to the direction of illumination and distributions at each point are anisotropic. Light distributions of op-

tically dense rubber eraser do not change with the incident angle. Additionally, distributions at each incident point are isotropic. For any material, angular distributions with the direction of illumination represent optical characteristics of the material.

In this section, we analyze the sampled BSSRDFs by visualization. If the BSSRDF is represented by an approximated low-dimensional function, it is difficult to analyze both spatial and angular distributions simultaneously. We carry out detailed analysis by sampling the full-dimensional BSSRDF.

4.3 Decomposition of isotropic and anisotropic components

To analyze light transport on an object surface, it is important to decompose the observed phenomenon into basic optical components. As traditional photometric methods have assumed only diffuse reflection, surface reflection is often decomposed into diffuse and specular reflection components to remove specular effect [44]. Nishino et al. [45] focused on the angular dependency of surface reflection, and decomposed surface reflection into angular dependent specular reflection and angular independent diffuse reflection. Inspired by their method, we decompose the observed BSSRDF according to the angular dependency.

In the previous section, we showed various directional dependencies of the scattered light; *i.e.*, the BSSRDF can be decomposed into an angular independent isotropic component and angular dependent anisotropic component as illustrated in Fig. 9. The isotropic component does not depend on the viewing direction, while the anisotropic component varies according to the viewing direction. Hence, we formulate the decomposition as

$$f(\mathbf{x}_i, \omega_i, \mathbf{x}_o, \omega_o) = f_i(\mathbf{x}_i, \omega_i, \mathbf{x}_o) + f_a(\mathbf{x}_i, \omega_i, \mathbf{x}_o, \omega_o), \quad (2)$$

where the function f_i represents the isotropic component and the function f_a represents the anisotropic component. It is noted that the argument ω_o is not included in the function f_i because of the independency on the viewing direction.

The two components are decomposed according to the constancy of the angular distribution. To implement this idea, we refer to a separation method proposed by Nishino *et al.* [45]. In their work, they simply extracted view-independent components by taking the minimal pixel value at each surface point as a constant component over image sequences. We also apply this idea to decompose sampled BSSRDFs. The isotropic component is separated by finding the minimal value along viewing directions at each surface point:

$$f_i(\mathbf{x}_i, \omega_i, \mathbf{x}_o) = \min_{\omega_o \in \Omega} f(\mathbf{x}_i, \omega_i, \mathbf{x}_o, \omega_o), \quad (3)$$

where Ω denotes the hemispherical directions. The anisotropic component is then computed as the residual according to

$$f_a(\mathbf{x}_i, \omega_i, \mathbf{x}_o, \omega_o) = f(\mathbf{x}_i, \omega_i, \mathbf{x}_o, \omega_o) - f_i(\mathbf{x}_i, \omega_i, \mathbf{x}_o). \quad (4)$$

An overview of this decomposition is depicted in Fig. 10.

Figure 11 shows the decomposition results of sampled BSSRDFs of epoxy resin, rubber eraser and marble in pseudo color. The left column shows the sum of sampled BSSRDFs for all observation directions E_{both} , the center column shows the sum of the decomposed anisotropic BSSRDF for all observation directions

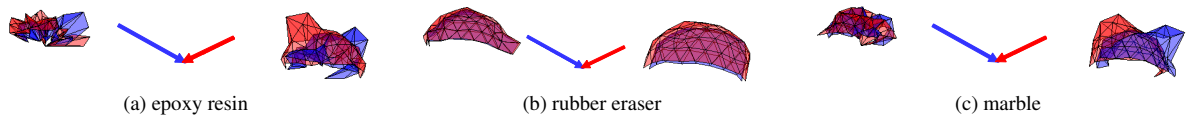


Fig. 8 Close up of the visualized BSSRDF, showing the angular distribution at $(x_o, y_o) = (-10, 0), (10, 0)$. The red arrow represents the direction of illumination $(\theta_i, \phi_i) = (44.3^\circ, 127.2^\circ)$ and the blue arrow represents the direction of illumination $(\theta_i, \phi_i) = (43.7^\circ, 233.7^\circ)$. Blue and red distributions represent the visualized angular distribution for each illumination

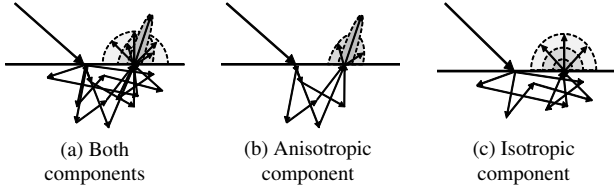


Fig. 9 Concept of decomposition. We decompose sampled BSSRDFs into isotropic and anisotropic components according to the directional dependency.

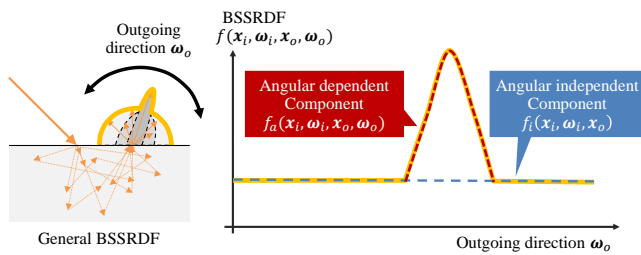


Fig. 10 BSSRDF decomposition with analysis of outgoing direction ω_o . Constant bias in the BSSRDF corresponds to an angular independent component, and the remainder of the BSSRDF is the component dependent on angle.

E_a and the right column shows the scaled decomposed isotropic BSSRDFs E_i , which are expressed as

$$E_{both} = \sum_{\omega_o} f(x_i, \omega_i, x_o, \omega_o), \quad (5)$$

$$E_a = \sum_{\omega_o} f_a(x_i, \omega_i, x_o, \omega_o), \quad (6)$$

$$E_i = s f_i(x_i, \omega_i, x_o). \quad (7)$$

As epoxy resin has strong directional scattering, most of the light is categorized in the anisotropic component. In contrast, strong multiple scattering in the rubber eraser belongs to the isotropic component. Illuminated light gradually loses its directionality as light scatters in the medium because the light path varies according to a number of scattering, such that low-bounce scattering retains the directionality, while higher-order scattering loses the directionality of a propagating light in the media. Hence, we often see anisotropic scattering in optically thin media and isotropic scattering in optically dense media. This result shows that we can decompose the scattering component into low-bounce and high-order scatterings according to the angular dependency, and the angular dependency is a clue with which to analyze optical density. Marble also has a low isotropic component because its inhomogeneous structure generates angular varying distribution. This result reveals that the spatial structure of an object affects the angular dependency of scattered light in the media.

From the above results of decomposition, we confirm that the sampled BSSRDFs can be decomposed into isotropic and anisotropic components by the analysis of the BSSRDF in out-

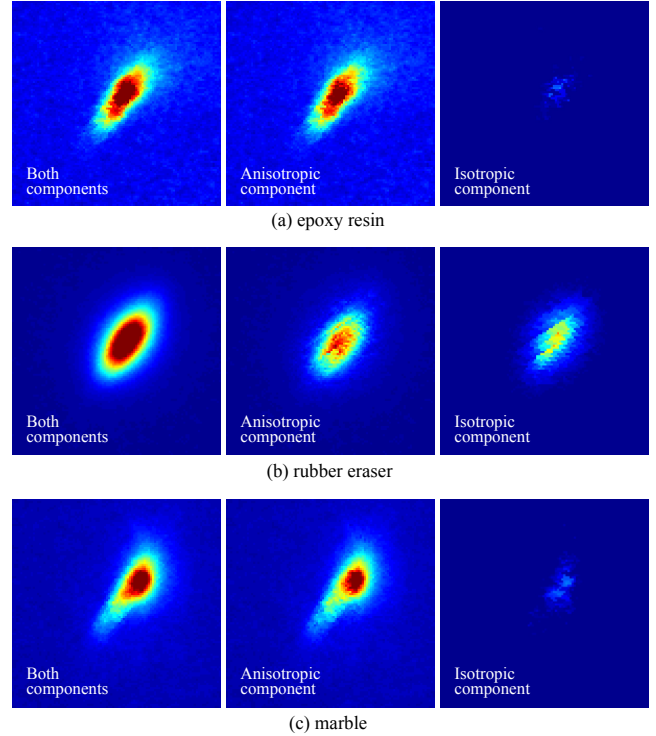


Fig. 11 Decomposition results for three materials. The left column shows both components, the center column shows the decomposed anisotropic component and the right column shows the decomposed isotropic component. Each image shows the total energies of emitted light at each surface point.

going direction. In addition, we can analyze optical thickness and homogeneity using the decomposed BSSRDF.

4.4 Discussion

In this section, we presented a novel method of sampling and analyzing full-dimensional BSSRDFs. For sampling, we used the *Turtleback reflector*, which is a polyhedral mirror system that illuminates and observes the object surface from various directions by virtual projectors and cameras. This system samples the full-dimensional BSSRDF in relatively short time. For analysis, we visualized spatial and angular distributions by slicing BSSRDFs with fixed incident light ray and direction of outgoing direction. The analysis on directional distributions of the light transport has already done in research on BRDFs, the analysis on incident and outgoing points is achieved by the full-dimensional BSSRDF. In addition, we decomposed the BSSRDF into angular isotropic and anisotropic components by the analysis of outgoing direction. The analysis revealed that the ratio of the two components strongly depends on the optical thickness and homogeneity of the medium.

5. Shape Estimation of an Optically Thin Translucent Objects

From this section, we propose a shape estimation method for a translucent object based on the discussion in Sec. 4.4. When traveling through a translucent medium, light collides with particles and scatters in the medium. Because the density of particles is low in optically thin translucent media, incident light rarely collides with particles and travels almost in a straight line. Thus, attenuated light is often observed around refracted light as shown in Sec. 4.2. The attenuation of light is modeled using the Lambert-Beer law [46]. The law describes that incident light exponentially attenuates along the length of the light path in a medium. While the light path of scattering is usually complex owing to uncountable collisions with particles, the light path of a single scattering is identified uniquely because light collides with a particle only once in the medium. Propagating light in an optically thin medium is dominated by low-bounce scattering, and the light attenuation model of single scattering is thus appropriate for our target. We derive a solution method using a model of single scattering that takes into account the refraction, an extinction coefficient and a phase function. Additionally, we develop an effective solution method based on energy minimization for the simultaneous estimation of the shape and scattering parameters.

5.1 Background

Figure 12 (a) shows a parametric single scattering model. In a scattering medium, incident light exponentially attenuates along the length of the light path according to the Lambert-Beer law [46]. It also scatters through a solid angle in the medium, and a good approximation of the phenomenon is the Henyey-Greenstein phase function [47]. With this phase function, the observed intensity I of single scattering is described as [14], [15]

$$I = sp(g, \theta)e^{-\sigma_r(d_1+d_2)} d\omega, \quad (8)$$

$$p(g, \theta) = \frac{1}{4\pi} \frac{1-g^2}{(1+g^2-2g\cos\theta)^{\frac{3}{2}}}, \quad (9)$$

where s is a scaling constant that includes the intensity of the incident light and scattering coefficient, σ_r is an extinction coefficient, $(d_1 + d_2)$ is the length of the light path in the medium, $d\omega$ is the solid angle of the light ray, and $p(g, \theta)$ is the phase function. The phase function represents the scattering distribution, and the distribution profile is controlled by a parameter g ($-1 \leq g \leq 1$). Fig. 12 (b), (c), and (d) show examples of the distribution profiles produced by varying g .

5.2 Formulation

We formulate the relationship between observed intensities of single scattering and the shape of a translucent target. Figure 13 shows our setting for the shape measurement. A translucent object is illuminated from one side and observed from the top. We assume a homogeneous material as a target object and orthographic projection for both illumination and observation. We also assume that an incident light ray attenuates along horizontal line in an object and does not reflect on other surfaces of the object. In addition, we ignore multiple scattering for now, but explain a

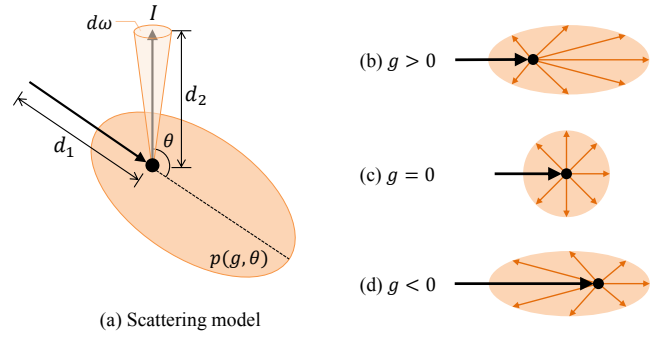


Fig. 12 Illustration of the scattering model and examples of distribution profiles with a varying phase function.

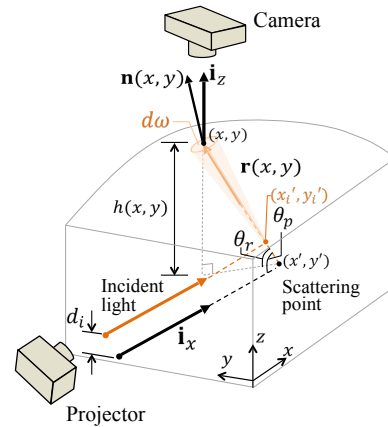


Fig. 13 Setting for shape estimation. A translucent object is illuminated from the side and observed from the top. Light path in the target object. The incident plane is almost planar, and incident light is assumed to be parallel to the x -axis. The illuminated ray reaches the surface point (x, y) , changing its travel direction at the scattering point (x', y') .

method for handling it in later sections.

Figure 13 illustrates a light path of single scattering in a medium. The incident ray \mathbf{i}_x scatters through a solid angle $d\omega$ at scattering point (x', y') , and reaches surface point (x, y) . $\mathbf{n}(x, y)$ represents the surface normal and $\mathbf{i}_x = [1, 0, 0]^T$ and $\mathbf{i}_z = [0, 0, 1]^T$ are incident and exiting light vectors, respectively. $\mathbf{r}(x, y)$ is a unit scattering vector pointing from the scattering point (x', y') to the surface point (x, y) . The angle between the incident vector \mathbf{i}_x and the scattering vector $\mathbf{r}(x, y)$ is denoted as θ_p . θ_r represents the projected angle of θ_p on the plane spanned by $\mathbf{r}(x, y)$ and \mathbf{i}_z . Our purpose is to estimate the height of the translucent object $h(x, y)$ from the observed intensity $I(x, y)$ at the surface point (x, y) on the surface, where the height of the incident ray is $z = 0$. The scattered incident ray \mathbf{i}_x is finally refracted at the object surface. The angle of refraction obeys Snell's law, expressed as

$$\mathbf{n}(x, y) \times \mathbf{i}_z = \eta \mathbf{n}(x, y) \times \mathbf{r}(x, y), \quad (10)$$

where η is the refractive index, and \times represents a cross-product operator. The total length of the light path becomes the sum of x' , which corresponds to the sum of the distance from the incident point to the scattering point and the distance from the scattering point to the surface point, $h(x, y)/\sin\theta_r$. As the intensity of single scattering is modeled as Eq. (8), the observed intensity is expressed as

$$I(x, y) = s F_t^{in} F_t^{out}(x, y) p(g, \theta_p) e^{-\sigma_t (x' + \frac{h(x, y)}{\sin \theta_r})} d\omega(h(x, y), \theta_r), \quad (11)$$

$$d\omega(h(x, y), \theta_r) = \frac{\sin \theta_r dA}{h(x, y)^2},$$

where s is a scaling constant, $F_t^{out}(x, y)$ is the Fresnel transmittance on the surface point (x, y) , and F_t^{in} is the constant Fresnel transmittance on the incident point because the incident light is perpendicular to the incident plane. dA is the physical size of a pixel in the observed image. Equation (11) shows that the observed intensity depends on both the geometric shape and scattering parameters, namely the extinction parameter σ_t , refractive index η , and phase function parameter g . Given these scattering parameters, the height of the translucent object is determined to an unknown offset owing to s as

$$h(x, y) = \frac{\sin \theta_r}{\sigma_t} \left(\log s + \log F_t^{in} + \log F_t^{out}(x, y) + \log p(g, \theta_p) + \log d\omega(h(x, y), \theta_r) - \log I(x, y) - x' \sin \theta_r \right). \quad (12)$$

5.3 Solution method

In the previous section, we described a basic theory for obtaining the shape from single scattering. However, in reality, we cannot directly estimate the object height $h(x, y)$ using Eq. (12) because of the unknown parameters and unclosed form of the function. In addition, the observed intensities include contributions from not only single scattering but also multiple scattering. In this section, we discuss a method that solves these problems. Our method assumes that the refractive index η is known because it can be directly measured using a refractometer.

Shape estimation by energy minimization

In our method, we employ an energy minimization approach to simultaneously determine both the shape and scattering parameters. When the unknown parameters and height are correctly estimated, Eq. (11) should give an intensity that is equivalent to the observed intensity $I(x, y)$. Although we can estimate the unknown parameters by seeking parameters that generate the observed intensity, parameter estimation tends to be unstable owing to a larger number of unknown parameters than the captured intensity. To reliably derive a solution to this problem, we use multiple $n(2 \leq n)$ images that are captured by changing the height of the incident ray; *i.e.*, we record multiple intensities $I_i(x, y)$ with varying heights of the incident rays $z = d_i$ ($i = 1, \dots, n$) as shown in Fig. 13. We now have n intensity observations per scene point $I_i(x, y)$, expressed as

$$I_i(x, y) = s F_t^{in} F_t^{out}(x, y) p(g, \theta_p) e^{-\sigma_t (x' + \frac{h(x, y) - d_i}{\sin \theta_r})} d\omega(h(x, y), \theta_r), \quad i = 1, \dots, n \quad (13)$$

We also take into account the signal-to-noise ratio of the observed intensities; the darker observations suffer more from image noise while the brighter observations are more reliable. We incorporate this by introducing a weighting factor w_i when determining the unknown parameters. We thus define an energy function for computing heights $h(x, y)$ and scattering parameters s, g, σ_t as

$$E(h(x, y), s, g, \sigma_t) = \sum_i w_i \sum_{x, y} \left(I_i(x, y) - I_i^{gen}(h(x, y), s, g, \sigma_t) \right)^2, \quad (14)$$

where I_i^{gen} is the generated intensity obtained using Eq. (13), and w_i is a weighting factor that reduces the effect of noise. We define the weighting factor w_i as

$$w_i = \frac{\sum_{x, y} I_i(x, y)}{\sum_{k=1}^n \sum_{x, y} I_k(x, y)}. \quad (15)$$

The energy function E evaluates the closeness between the observed intensity and intensity generated using Eq. (13). The minimization of the energy function E gives us estimates of the height $h(x, y)$ per-pixel and scattering parameters s, g and σ_t as

$$\{h(x, y), s, g, \sigma_t\} = \underset{h(x, y), s, g, \sigma_t}{\operatorname{argmin}} E(h(x, y), s, g, \sigma_t). \quad (16)$$

We describe the optimization method in the following section.

5.4 Implementation

This section describes the implementation details of the solution method. Our method employs non-linear optimization because of the non-convexity of Eq. (14) with respect to the unknown parameters. We now describe the method for making the initial guess of the height $h(x, y)$ and the following optimization strategy.

Estimation of initial shape: To make an initial guess of the estimated parameters, we use the initial shape $h^0(x, y)$ computed by ignoring refraction ($\eta = 1$). When $\eta = 1$, the scattering vector coincides with the output vector \mathbf{i}_z , the two-dimensional projection of the scattering point (x', y') becomes identical to the surface point (x, y) , and Fresnel transmittance $F_t^{out}(x, y)$ is constant because refraction is disregarded. Since the angle θ_p equals $\pi/2$, the phase function $p(g, \theta_p)$ becomes constant. In addition, we assume that solid angle $d\omega(h(x, y), \theta_r)$ is a constant value. The intensity generated from initial height $h^0(x, y)$ is described as

$$I_i^0(x, y) = S e^{-\sigma_t (h^0(x, y) + x - d_i)}, \quad S = s F_t^{in} F_t^{out} p\left(g, \frac{\pi}{2}\right) d\omega. \quad (17)$$

Here, unknown parameters are the height $h^0(x, y)$, scaling constant S , and extinction coefficient σ_t . Using a pair of intensity observations $I_i(x, y)$ and $I_j(x, y)$ obtained for different heights of incident rays d_i and d_j , the extinction coefficient is calculated as

$$\sigma_t = \frac{\log I_i(x, y) - \log I_j(x, y)}{d_i - d_j} \quad (d_i \neq d_j). \quad (18)$$

In practice, we take the average for all pairs of d_i and d_j as the estimate of σ_t . We employ the intensity at the incident point as the initial scaling constant S for the scaling without attenuation. The initial guess of the height $h^0(x, y)$ is therefore described as

$$h^0(x, y) = \frac{1}{\sigma_t} (\log S - \log I_i(x, y)) - x + d_i, \quad (19)$$

and is estimated using the parameters σ_t and S . We use this initial guess as an input to the optimization: $h(x, y) \leftarrow h^0(x, y)$.

Optimization: Now we estimate the shape and parameters by minimizing Eq. (16) using h^0 as the initial guess of the shape. The unknowns to be estimated are the per-pixel height $h(x, y)$ and

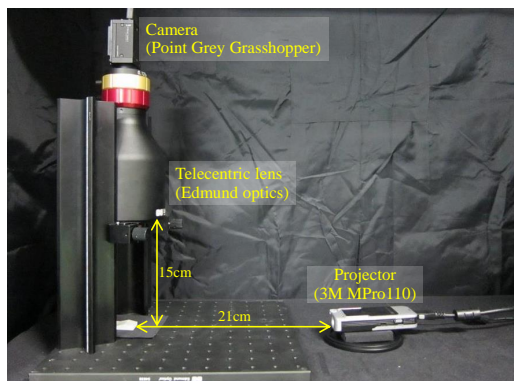


Fig. 14 Experimental setting. A projector is placed on the side of the object, and a camera is vertically placed. We used a telecentric lens for orthographic projection.

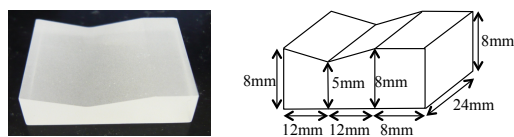


Fig. 15 Target object for evaluation

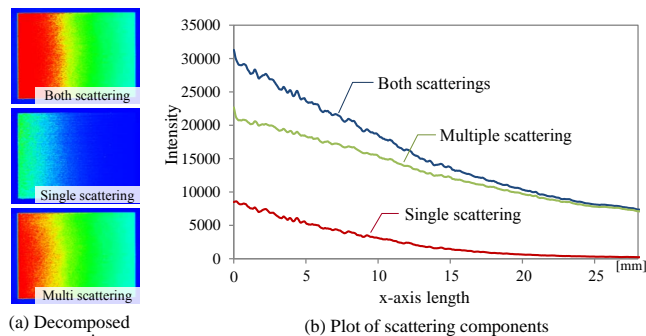
scattering parameters s , g , and σ_t . To efficiently avoid local minima, we use a two-step approach for the optimization. Specifically, we first apply particle swarm optimization [48] to limit the search range in a coarse manner, and then use the Nelder-Mead method [49] to find the optimal parameter set on a fine scale.

Extraction of single scattering: As discussed above, actual observations consist of both single and multiple scatterings. To separate the single scattering component from multiple scattering, we utilize a separation method [14] which uses projector as a light source as shown in 13. The extracted single scattering component is used as input for our method. Readers are referred to [14] for the details of the separation method.

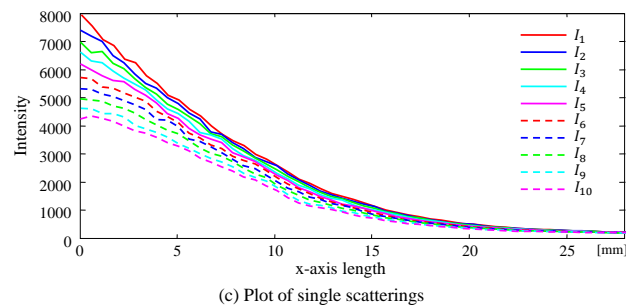
5.5 Experiments

We assess the effectiveness of the proposed method for real-world scenes. Figure 14 shows the experimental setting. A 3M MPro110 projector was placed on the side of the target object, and a Point Grey Grasshopper camera that had a linear response sensor was vertically placed to obtain a top view. To avoid the perspective effect of the imaging system, we used an Edmund optics telecentric lens for approximating an orthographic projection. To perform a comprehensive analysis, we used a concave translucent object which is made in known size. We show target objects and their sizes in Fig. 15. The ground truth of these objects was known for quantitative evaluation. We set the refractive index n as 1.3. We captured intensities of single scattering $I_i(x, y)$ ($d_i = 0.25 \times i$ [mm], $i = 0, \dots, 9$) while shifting the height of incident light.

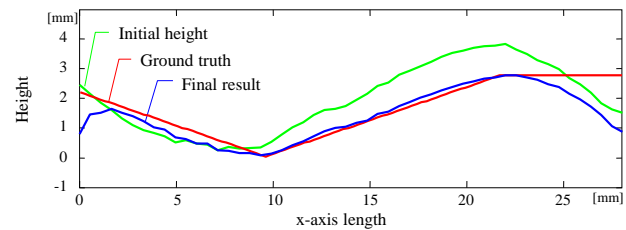
Figure 16 shows the experimental result for the concave object. Figure 16 (a) shows the decomposition of the scattering components in pseudo color. We also horizontally plot intensities of each scattering component in Fig. 16 (b). The red, green, and blue plots show the intensities of single scattering, multiple scattering, and observed scattering, respectively. It is observed that single scattering is almost exponentially attenuated with increas-



(a) Decomposed scattering (b) Plot of scattering components



(c) Plot of single scatterings



(d) Estimated shape

Fig. 16 Experimental result

ing distance from the incident point. Figure 16 (c) shows plots of extracted single scattering with for different heights of incident light. We estimate the target shape from these intensities. One-dimensional plots of estimation results are shown in Fig. 16 (d). The red, green, and blue lines are the ground truth, initial height, and final result, respectively. The initial height is not very far from the ground truth. The final result is estimated as being close to the ground truth. However, the final result is estimated incorrectly in the region of a planar surface. A possible reason for the incorrect estimation is insufficient intensity of single scattering for shape estimation because the light paths are longer in observing this region. In addition, the shape near the incident plane does not match the ground truth well owing to the bright observation at the incident point and its glare. Scattering parameters are estimated as $s = 1.21 \times 10^4$, $g = 0.042$, and $\sigma = 0.132[\text{mm}^{-1}]$.

We show the result of another convex scene in Fig. 17. Figure 17 (c) shows the reconstruction result given by single scattering with illumination from the front of the target object. Because of the insufficient intensities of single scattering as shown in Fig. 17 (b), the estimated height has large error in the back area. To reduce the error, we capture the intensities of single scattering by illuminating from the other side of the target object, and then merge the two estimated reconstruction results. Figure 17 (d) shows the merged result. Large noise is reduced and whole the shape is estimated. However, estimated surfaces are not planar due to artifacts in the decomposed single scattering as shown in

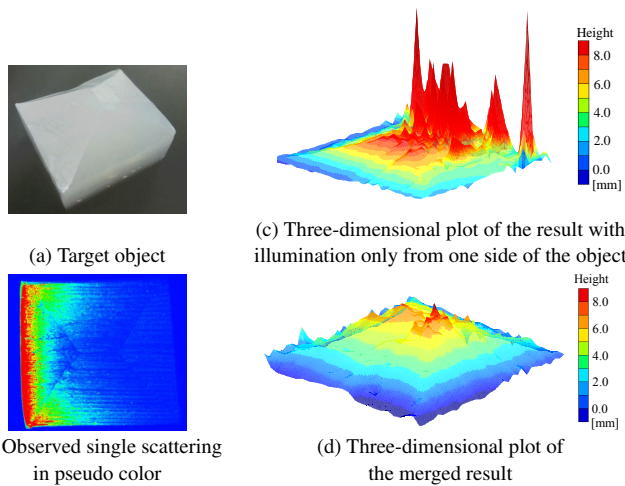


Fig. 17 Experimental results for an asymmetric convex scene. (b) Observed single scattering in pseudo color. (c) Three-dimensional plot of the estimation result with illumination only from one side of the object. (d) Three-dimensional plot of the merged result.

Fig. 17 (b). This artifact is occurred by projected high-frequency stripe pattern. It remains difficulty on separation of scattering components with high accuracy.

5.6 Discussion

Computation time: In this experiment, it took about 15 minutes to capture images (six images for extracting single scattering at each of 10 different depths), and it takes a few hours to compute the shape with an unoptimized Matlab implementation. We computed estimates on an Intel Core 2 Duo central processing unit (3.00 GHz) with 3GB random access memory. The size of the problem is 259 (256 points for $h(x, y)$, s , g , and σ_r) in symmetric real data, and 873 (870 points for $h(x, y)$, s , g , and σ_r) in asymmetric real data.

Limitations: There are a few limitations to the current method. These limitations will be overcome in our future work.

- **Object shape:** Our current formulation requires that the incident plane is planar and incident light on the target object is parallel to the x-axis for the extraction of single scattering using high-frequency projection. When projected patterns interfere with each other, single scattering cannot be extracted. This assumption needs to be relaxed when it is applied to a more general shape.
- **Single scattering in an inhomogeneous material:** As our method uses single scattering, which exponentially attenuates with constant scattering parameters, we cannot estimate the shape of an inhomogeneous material. To deal with spatially varying scattering media, it is required to estimate scattering parameters in a three-dimensional volume. However, estimation of a huge number of unknown scattering parameters is a challenging task.

5.7 Summary

In this section, we proposed a method of estimating the shape of optically thin translucent objects based on the attenuation of single scattering. Because the light in optically thin translucent object is dominated by low-bounce scattering, the attenuation

model of single scattering is appropriate for target objects in this section. We modeled the light attenuation in the object based on Lambert-Beer law and make relationship between the shape of target object and observed intensities of single scattering. Experiments with real-world results demonstrated that our method has the potential for the accurate modeling of translucent objects, which has been difficult to achieve with other appearance-based methods. While the method works well for translucent objects, the accuracy suffers from low-intensity measurements and a high signal-to-noise ratio when measuring optically thick objects, for which multiple scattering dominates the appearance. In addition, the accuracy of shape estimation depends on quality of extracting single scattering by high-frequency illumination. Another issue relating to the current approach is the high computational cost. We are interested in looking into these aspects further to make the approach more practical.

6. Shape Estimation of an Optically Thick Translucent Objects

The shape of the optically thin translucent object is estimated from single scattering, which is attenuated along the refracted light. Refracted light is useful in reconstructing the object shape because it depends directly on the surface direction. By contrast, in optically thick translucent objects, incident light does not propagate along the refractive direction, but rather distributes around the incident point owing to uncountable collisions with particles in the medium as described in Sec. 4.2. As a result, we cannot observe refractive transmitted light in the medium but rather obtain shading of the target object. Observed shadings are often used to estimate surface normals, which represent the direction of the object surface, in a photometric stereo technique [24]. The photometric stereo technique is known as a method of estimating object shape from multiple shading images. While conventional photometric stereo methods have been developed for simple Lambertian diffuse surfaces [39], recent generalizations can handle more complex reflections in real-world scenes [50], [51]. However, the estimation of the surface normals of translucent materials remains a difficult task, with subsurface scattering being significant [52].

While the exact modeling of subsurface scattering remains a difficult task that requires complicated models, prior studies in the field of computer graphics show that the image formation model of subsurface scattering can be well approximated as the convolution of the scattering kernel and surface radiance of optically thick materials, which distribute light regardless of the incident direction [53]. In Sec. 4, we show that light transport in an optically thick translucent medium does not depend on the directions of the incident and outgoing light. Hence, we use this approximation to develop *surface normal deconvolution*, which recovers the original surface normal from the *blurry* surface normal obtained by applying the conventional photometric stereo method to translucent objects. This idea is similar to Dong *et al.*'s method [54], which estimates the surface normal using deconvolved input images to remove the subsurface scattering effect. While Dong *et al.* assumed parametric subsurface scattering (*i.e.*, photon beam diffusion of optically homogeneous media), we represent subsurface scattering by non-parametric convolution kernels for either opti-

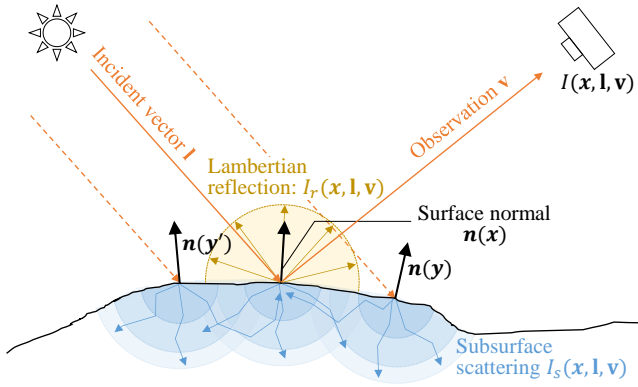


Fig. 18 Light interactions on a translucent surface. Incident light is partially reflected from the surface, while the remaining light transmits and spreads inside the subsurface.

cally homogeneous or inhomogeneous media. The convolution kernels can be either calibrated or estimated, and various deconvolution techniques in the literature (such as image deblurring methods) can be used in the implementation to recover the deblurred surface normal. We present estimation results obtained using our deconvolution formulation and using existing deconvolution in experiments.

6.1 Convolutional Image Formation Model

We begin with the image formation model for a translucent surface. When light illuminates a translucent surface, it is reflected, transmitted and absorbed as depicted in Fig. 18. A portion of the transmitted light returns to the surface via subsurface scattering; thus, the radiance $I(x, \mathbf{l}, \mathbf{v})$ at a scene point x with incident vector \mathbf{l} and observation vector \mathbf{v} becomes the sum of the reflection $I_r(x, \mathbf{l}, \mathbf{v})$ and subsurface scattering $I_s(x, \mathbf{l}, \mathbf{v})$ components:

$$I(x, \mathbf{l}, \mathbf{v}) = I_r(x, \mathbf{l}, \mathbf{v}) + I_s(x, \mathbf{l}, \mathbf{v}). \quad (20)$$

The subsurface scattering component $I_s(x, \mathbf{l}, \mathbf{v})$ is modeled as [17]

$$I_s(x, \mathbf{l}, \mathbf{v}) = \gamma(x) F(\mathbf{v}, \mathbf{n}(x), \eta) \int_{y \in A} R(x, y) F(\mathbf{l}, \mathbf{n}(y), \eta) \mathbf{n}(y)^T \mathbf{l} dy, \quad (21)$$

where $\gamma(x)$ is a scale factor for the subsurface scattering component, F represents Fresnel transmission, and $\mathbf{v}, \mathbf{n}, \mathbf{l} \in \mathbb{R}^3$ are the observation, surface normal, and incident vectors, respectively. η is a refractive index, $R(x, y)$ represents an extinction term for light traveling from scene point x to its neighbor y such as a dipole model [17], and A defines a neighboring area. Generally, the subsurface scattering component describes a nonlinear relation between the surface normal and observed intensity owing to the Fresnel transmission term. To relax this complexity, we approximate the original model as a simpler form by assuming an optically thick material, as in [55]. On the surface of an optically thick material, subsurface scattering does not depend on the direction of the light, because the transmitted light scatters uncountable times and loses its directionality due to random light paths as in the diffusion approximation. Thus, subsurface scattering is invariant to the incident direction and outgoing direction, and the Fresnel term F can be regarded as constant for an optically thick material. As a result, the subsurface scattering component

$I_s(x, \mathbf{l}, \mathbf{v})$ is simplified as

$$I_s(x, \mathbf{l}) = \gamma'(x) \int_{y \in A} R(x, y) \mathbf{n}(y)^T \mathbf{l} dy, \quad (22)$$

where $\gamma'(x)$ is a new scale factor of subsurface scattering that includes constant Fresnel transmission terms.

Assuming a Lambertian reflectance model for the reflection component

$I_r(x, \mathbf{l}) = \rho(x) \mathbf{n}(x)^T \mathbf{l}$ with a diffuse albedo $\rho(x)$, the intensity observation $I(x, \mathbf{l}, \mathbf{v})$ can be written as

$$I(x, \mathbf{l}) = \left[\rho(x) \mathbf{n}(x) + \gamma'(x) \int_{y \in A} R(x, y) \mathbf{n}(y) dy \right]^T \mathbf{l}. \quad (23)$$

The first factor of Eq. (23) can be regarded as a simple convolution model as

$$I(x, \mathbf{l}) = \left[\int_{y \in A} h(x, y) \mathbf{n}(y) dy \right]^T \mathbf{l} = (h * \mathbf{n}(x))^T \mathbf{l}, \quad (24)$$

where $*$ is the convolution operation, and the kernel h represents a scattering effect for the surface normals and is expressed as

$$h(x, y) = \rho(x) \delta(x - y) + \gamma'(x) R(x, y). \quad (25)$$

The kernel h expresses the spatial attenuation of scattering from incident point on the object surface.

A similar convolutional approximation of subsurface scattering is also discussed in the work of Munoz *et al.* [55] for the forward rendering of optically thick materials. This method is inspired by the works of convolutional approximated subsurface scattering by d'Eon *et al.* [56] for the rendering of human skin and Donner *et al.* [41] for multi-layered materials. Unlike their method, where the extinction term $R(x, y)$ is defined as a function parameterized only by the relative positions of x and y , our method allows more flexibility for the extinction term $R(x, y)$ so that inhomogeneous translucent materials can also be handled.

6.2 Solution method

Based on the convolutional image formation model, we develop a photometric stereo method for estimating the surface normals of an optically thick translucent surface. Our input is the same as that of the traditional photometric stereo method in that a set of images is taken under varying lighting directions from a fixed viewpoint. To simplify the discussion, we assume that the light directions are calibrated and the observations do not include shadows. In the rest of the paper, we consider the discretized pixel sites u and v that correspond to scene points x and y , respectively; thus, Eq. (24) becomes

$$I(u, \mathbf{l}) = (h(u, v) * \mathbf{n}(u))^T \mathbf{l}. \quad (26)$$

The convolution equation Eq. (26) has the simple linear algebraic expression

$$\mathbf{D} = \mathbf{HNL}, \quad (27)$$

where $\mathbf{D} \in \mathbb{R}^{m \times k}$ is an observation matrix, m and k are the numbers of pixels and light directions, respectively, $\mathbf{H} \in \mathbb{R}^{m \times m}$ is

a scattering matrix, $\mathbf{N} \in \mathbb{R}^{m \times 3}$ is a surface normal matrix, and $\mathbf{L} \in \mathbb{R}^{3 \times k}$ is an incident light matrix, which is assumed to be known. This linear expression indeed has similarity to the expression of the Lambertian photometric stereo method [24], where the observation \mathbf{D} , scaled surface normal \mathbf{N}_s , and light matrix \mathbf{L} have the relationship

$$\mathbf{D} = \mathbf{N}_s \mathbf{L}. \quad (28)$$

From Eqs. (27) and (28), we see that the scaled surface normal \mathbf{N}_s corresponds to \mathbf{HN} according to

$$\mathbf{N}_s = \mathbf{HN}. \quad (29)$$

Therefore, we can regard the scaled surface normal \mathbf{N}_s as a *blurry* version of the original surface normal \mathbf{N} that we wish to estimate. In the following, we call \mathbf{N}_s a smoothed surface normal.

We estimate the surface normal \mathbf{N} by taking the following two-step approach. (a) Obtain the smoothed surface normal \mathbf{N}_s by Lambertian photometric stereo [24], (b) Estimate the surface normal \mathbf{N} in a deconvolution framework using the subsurface scattering matrix \mathbf{H} .

(a) Estimation of the smoothed surface normal \mathbf{N}_s .

We use a conventional Lambertian photometric stereo method [24] to derive the smoothed surface normal \mathbf{N}_s as

$$\mathbf{N}_s = \mathbf{DL}^\dagger, \quad (30)$$

where † represents a Moore-Penrose pseudo inverse.

(b) Estimation of the original surface normal \mathbf{N} .

Once the smoothed surface normal \mathbf{N}_s is obtained, we use Eq. (29) to derive the original surface normal \mathbf{N} . If the scattering matrix \mathbf{H} is available and invertible, we can directly obtain the estimate of the original surface normal \mathbf{N} in a linear least-squares fashion as $\mathbf{N} = \mathbf{H}^{-1}\mathbf{N}_s$. As the estimation result produced by such simple deconvolution is often degraded by ringing artifacts owing to the loss of high-frequency information in the original signal, we use a smoothness constraint to stabilize the estimation. We design the smoothness term s as a weighted second-order difference of $\mathbf{n}(u)$ between u 's neighborhood locations t and v as

$$\mathbf{n}''(u) = w(t, u) (\mathbf{n}(t) - \mathbf{n}(u)) - w(u, v) (\mathbf{n}(u) - \mathbf{n}(v)). \quad (31)$$

The weight $w(u, v)$ controls the discontinuity of surface normals by taking the difference of intensity observations across varying lightings \mathbf{l}_i as

$$w(u, v) = \exp \left(-\frac{1}{m} \sum_i^k (I(u, \mathbf{l}_i) - I(v, \mathbf{l}_i))^2 \right). \quad (32)$$

The matrix expression of the smoothness \mathbf{N}'' is given as

$$\mathbf{N}'' = \mathbf{WN}, \quad (33)$$

where $\mathbf{W} \in \mathbb{R}^{a \times m}$ is a matrix of the second-order derivative filter, and a is the number of triplets used to compute the second-order derivatives. In our case, we define the triplets along horizontal and vertical directions in the image coordinates. Finally, our estimation problem becomes a ridge regression problem expressed as

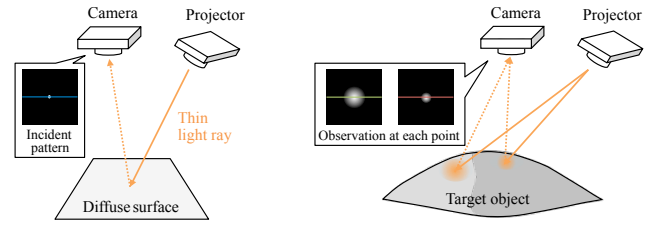


Fig. 19 Setting for measuring the convolution kernel. A projector casts a thin light ray on the target object. We estimate the convolution kernel from the incident pattern and light distributions on the target object. In the case of an inhomogeneous medium, we capture light distributions of optically different regions.

$$\hat{\mathbf{N}} = \underset{\mathbf{N}}{\operatorname{argmin}} \|\mathbf{HN} - \mathbf{N}_s\|_F^2 + \lambda \|\mathbf{WN}\|_F^2, \quad (34)$$

where λ controls the smoothness of the estimates. An explicit solution to this problem is given by setting the first-order derivative to zero as expressed by

$$\mathbf{N} = (\mathbf{H}^T \mathbf{H} + \lambda \mathbf{W}^T \mathbf{W})^{-1} \mathbf{H}^T \mathbf{N}_s. \quad (35)$$

In this manner, the estimates for the original surface normal \mathbf{N} can be obtained in a closed-form.

The mathematical expression of the problem is equivalent to that of the image deblurring problem, where the original sharp image is recovered via deconvolution. The important difference, however, is that our problem deals with the deconvolution of surface normals. Therefore, conventional image priors that are developed for natural images may not be suitable. Other than this aspect, existing deconvolution techniques can be alternatively used to estimate the surface normal \mathbf{N} from the smoothed surface normal \mathbf{N}_s . The convolution kernel \mathbf{H} is generally unknown, but can be either calibrated (non-blind deconvolution) or estimated (blind deconvolution). While most image deblurring techniques are limited to spatially invariant point spread functions (PSFs), which corresponds to handling optically homogeneous materials in our case, the formulation of Eq. (35) can naturally handle optically inhomogeneous materials, corresponding to the case of spatially-varying PSFs.

Calibration of the Convolution Kernel

As mentioned above, the surface normal deconvolution can be performed without knowing the convolution kernel using blind deconvolution techniques; however, knowledge of the convolution kernel is useful for stabilizing the estimation. In addition, spatially variant deconvolution is a challenging task in research on image deconvolution [57], [58]. Thus, we need to know convolution kernels at each position for dealing with optically inhomogeneous translucent objects. Here we describe a simple procedure for measuring the convolution kernel. Fig. 19 shows our setting for measuring the convolution kernel. By illuminating a diffuse surface and the target translucent material individually by a thin ray emitted from a projector, we obtain the measurements of the incident light distribution and scattering response on the surface, respectively. The measured scattering response corresponds to the convolution between the incident light distribution and the convolution kernel. From this relationship, we calibrate the convolution kernel h which represents spatial attenuation of scattering. When the target medium is optically inhomogeneous,

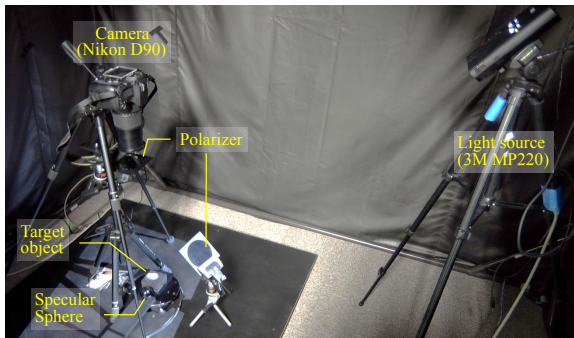


Fig. 20 Experiment setting and target objects. We used a projector as a light source. The camera was equipped with a telescopic lens. Polarizers were used to reduce the effects of specular reflection on the target object.

we need to calibrate the convolution kernel in each optically different region.

6.3 Experiments

We now evaluate our method using real-world data for the purposes of qualitative evaluations. Figure 20 shows our experiment setting. We used a Nikon D90 camera with a linear radiometric response function (RAW mode) and a telescopic lens to approximate an orthographic projection. We used a 3M MP220 projector to provide illumination. The target scenes are illuminated under directional lighting, and the light directions are calibrated using a dark specular sphere. In addition, to avoid specular reflections from the scene, we placed polarizers in front of both the light source and camera. We used two target objects: a bar of soap as a homogeneous medium and unicorn ornaments as an inhomogeneous media. Each scene was recorded for 12 different lighting directions. The image sizes of the soap and unicorn scenes were 232×164 and 158×230 pixels, respectively. Prior to the measurement, the convolution kernels were measured using the procedure described in Sec. 6.2. For the inhomogeneous objects, we measured two distinct kernels for the different material regions, one for a white region and the other for a pink region.

Figure 21 shows the experimental results for the soap. The recorded intensity image is not notably blurry, but the details are smoothed by subsurface scattering as shown in Fig. 21 (a). The observed PSF shows incident light distributed on the surface of the soap. Figure 21 (b) shows the surface normals estimated using the Lambertian photometric stereo method [24] and our method. While the result of the Lambertian photometric stereo method shows smoothed surface normals, our result is sharper. We also reconstruct the surface shape from normals estimated using Agrawal *et al.*'s method[59] as shown in Fig. 21 (c). We recognize that detailed shapes can be estimated from the normals of our method.

Figure 22 show experimental results for the unicorn. Observed PSFs have different light distributions for the different materials as shown in Fig. 22 (a). Although the observed image is blurred compared with decomposed direct image, our method estimates sharper surface normals by reducing scattering effects.

6.3.1 Discussion

Computation time: In the case of optically homogeneous materials, we can apply various fast deconvolution methods for image

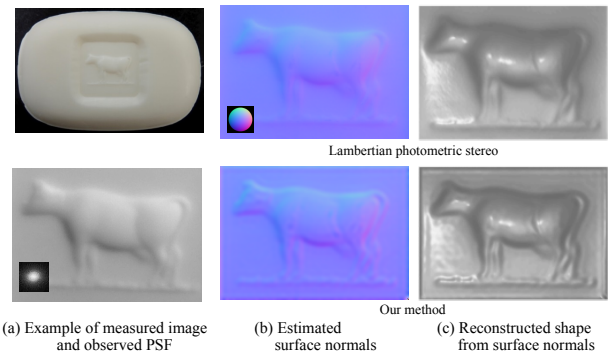


Fig. 21 Result for a real-world scene of soap as a homogeneous medium. The direct image is calculated using Gu *et al.*'s method[60], and shapes are reconstructed using Agrawal *et al.*'s method [59].

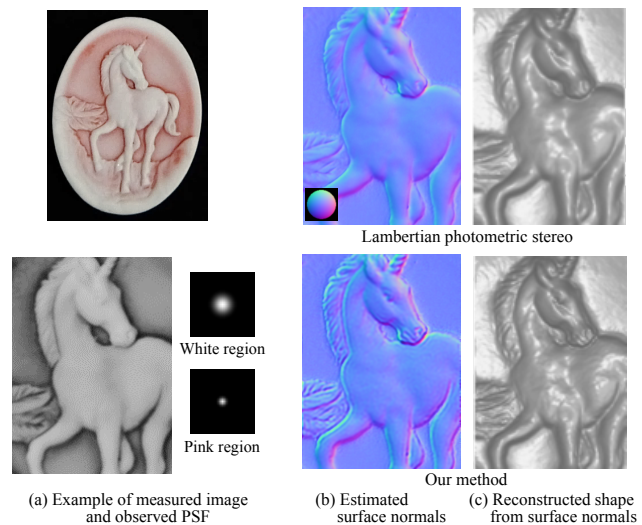


Fig. 22 Result for a real-world scene of a unicorn ornament as an inhomogeneous medium.

deblurring to recover the surface normal. However, in the case of inhomogeneous media, we have to solve Eq. (35) to deal with spatially variant convolution kernels. Our Matlab implementation on an Intel Core i7 central processing unit (3.5 GHz) takes about 17.6 and 3.5 seconds to recover the surface of the soap and unicorn scenes, respectively. The density of non-zero elements of matrix $\mathbf{F}^T \mathbf{F} + \lambda \mathbf{W}^T \mathbf{W}$ in Eq. (35) is about 2.5%. The computation time depends on the size and number of non-zero elements of matrix $\mathbf{F}^T \mathbf{F} + \lambda \mathbf{W}^T \mathbf{W}$, which are determined by the input image size and apparent sizes of PSFs in the image coordinates.

Limitations: Our method has a couple of limitations. First, we have ignored the effect of Fresnel transmissions. Thus, our method is restricted to optically thick materials. As a material has directional scattering, the accuracy of our method may gradually decrease. We are interested in exploring an iterative estimation framework that can be used to adaptively update the convolution kernels for the incorporation of the Fresnel transmission effects. The second limitation is that our method in practice relies on known convolution kernels, especially when dealing with optically inhomogeneous materials. Although a sophisticated blind deconvolution method may resolve this issue, at this point, knowledge of the convolution kernel plays an important role in obtaining accurate surface normal estimates. We are inter-

ested in investigating good prior information for surface normal fields that may potentially improve the blind deconvolution.

6.4 Summary

In this section, we proposed a shape estimation method for optically thick translucent objects. As optically thick translucent objects show shading on their surfaces, we estimate surface normals as the object shape from observed images employing the photometric stereo method. We extended the previous study on the convolutional approximation of subsurface scattering and developed a surface normal deconvolution technique, which consists of a conventional photometric stereo method and image deconvolution. Our experiment shows that the surface normals of translucent objects are reliably estimated by our method. In addition, we showed that our method is able to deal with optically inhomogeneous media.

7. Summary and Discussions

In this thesis, we proposed methods of estimating the shape of translucent objects from observed scattering light according to light transport analysis. Scattering in translucent media adversely affects shape measurement because it prevents reference to the reflection on object surface. While most existing methods extract the scattering effect and thus ignore complex phenomena, scattering is not completely reduced owing to the degree of the spatial distribution [13]. Our *shape from scattering* framework tackles these problems by obtaining the object shape from the observed scattering effect itself. The key concept is how to model the relationship between the observed scattering effect and shape of the target object. Scattering observations depend not only on the target shape but also on the optical characteristics of the medium. Hence, we developed an approximation model of subsurface scattering according to the analysis of light transport in a real translucent medium.

First, we measured light transport in real translucent objects as described in Sec. 4. We used the *Turtleback Reflector* to distribute virtual illuminations and observations around the target scene, and captured the light transport as the eight-dimensional BSSRDF that is parameterized by the directions and positions of incident and outgoing light. The captured BSSRDF was visualized as a distribution around the outgoing direction at each outgoing point with fixed illumination for the analysis of the behavior of light transport. We also decomposed the BSSRDF into directional and nondirectional components by analyzing the BSSRDF along outgoing directions. As a result, we obtained the characteristics of the response of the BSSRDF to optical properties such as the directional light in an optically thin translucent medium, directionally invariant light in optically thick translucent objects, spatially invariant light in a homogeneous medium, and spatially varying light in an inhomogeneous medium. While reflection analysis of the outgoing direction is conducted using the four-dimensional BRDF, spatial analysis of light transport is available using the eight-dimensional BSSRDF.

According to the discussion in Sec. 4, we constructed shape estimation methods for translucent objects. We related scattering observations and object shape with optical parameters, and

estimated the object shape from observations. For optically thin translucent objects, we used the attenuation model of single scattering to represent the directional light distribution around the refracted light in the medium. We formulated single scattering observed in the experimental setting as a function of object shape, and estimated object shape by minimizing an energy function, which evaluates the difference between observed and synthesized intensities. We evaluated the estimation accuracy of our method with real data, and showed the availability of our method when single scattering inputs are sufficiently bright. For optically thick translucent objects, we approximate non-directional scattering in the convolution model. This models not the direct relationship between the observed intensity and surface shape but the observed intensity and surface normals, which represent the direction of the object surface. Although the object shape needs to be reconstructed from the estimated normals, the convolution model provides a simple estimation process using a deconvolution algorithm. While we need to calibrate the scattering distribution on the target surface of each material, we can handle optically inhomogeneous media. Experiments employing real scenes were conducted to evaluate the effectiveness of deconvolution-based scattering reduction in our method.

Our proposal of the *shape from scattering* framework allows us to estimate a translucent shape from observed scattering itself without complicated light transport analysis. *Shape from scattering* extends shape estimation to a variety of targets having translucent appearance. Such extension could benefit a wide range of applications in the field of computer vision that require shape information; *e.g.*, the automatic visual inspection of industrial products and the archiving of artistic sculptures, where translucent objects are made of plastic, marble, and wax. Meanwhile, our framework can also be used in the application of medical imaging because target organs have strong scattering properties. On the microscope scale, the main application of our method would be cell imaging.

We still face the problem that our method works on only translucent objects whose scatterings are modeled as the attenuation of single scattering or non-directional multiple scattering. While we extracted single scattering component from scatterings in optically thin translucent objects, the single scattering does not always become a main component in scattering. In optically thin materials, low-bounce scatterings such as two and three-bounce scattering are also a main scattering component. Thus, even if the target object is relatively optically thin translucent, there is a possibility that extracted single scattering is insufficient intensity for shape estimation. The spatially varying optical properties of target objects are also limited in proposed shape estimation. In the method for optically thin translucent objects, we assume the spatially homogeneous material. This constraint allows us to estimate optical parameters such as extinction coefficient, however, we cannot apply this shape estimation method to optically inhomogeneous translucent object. On the other hand, in the method for optically thick translucent objects, we can handle optically inhomogeneous objects, but advancedly calibrated scattering kernels at each point on the object surface are needed. Simultaneous estimating the object shape and optical parameters of optically

inhomogeneous material is the most difficult problem setting.

The ultimate solution to deal with any type of translucency is a brute-force search via the simulation of light propagation in arbitrary translucent media without any parametric scattering models. However, it is an ill-posed problem to estimate spatially distributed optical properties and the object shape from a two-dimensional observed image in real time because a search range of an enormous number of unknowns is too huge to obtain an optimal solution. A conventional camera obtains only two-dimensional information, whereas recently developed advanced cameras can obtain richer information; e.g., the light field camera and ultrafast imaging camera [61]. The light field camera can store directions of incoming light from a scene, and the captured data then give the directional information of propagating light. Because the information of directionality relates to the directional distribution on BSSRDFs of a target object, the light field camera imaging helps to shrink the search range of shape estimation. Ultrafast imaging [61] observes the temporal sequence of light propagation at a trillion frames per second. Since this ultrafast speed competes with the speed of light, we see the process of the light propagation from the captured image sequence. In the field of computer graphics, realistic image is rendered by simulating the propagation of light rays. Therefore, temporal image sequence becomes a clue for inversely rendering of target scene. These rich information will allow us to analyze light transport and make it possible to obtain the shape of a general translucent material in the future.

Our *shape from scattering* framework contributes technique of photometric analysis in the field of computer vision in the terms of using scattering light for obtaining object shape.

References

[1] Healey, G. and Binford, T. O.: Local shape from specularity, *Computer Vision, Graphics, and Image Processing*, Vol. 42, pp. 62–86 (1987).

[2] Kutulakos, K. N. and Steger, E.: A theory of refractive and specular 3d shape by light-path triangulation, *Proc. of International Conference on Computer Vision* (2005).

[3] Miyazaki, D. and Ikeuchi, K.: Shape estimation of transparent objects by using inverse polarization raytracing, *IEEE Trans. on Pattern Analysis and Machine Intelligence*, Vol. 29, No. 11, pp. 2018–2030 (2007).

[4] Murase, H.: Surface shape reconstruction of a nonrigid transport object using refraction and motion, *IEEE Trans. on Pattern Analysis and Machine Intelligence*, Vol. 14, No. 10, pp. 1045–1052 (1992).

[5] Godin, G., Rioux, M. and Beraldin, J. A.: An assessment of laser range measurement on marble surfaces, *Conference on Optical 3D Measurement Techniques* (2001).

[6] Holroyd, M. and Lawrence, J.: An analysis of using high-frequency sinusoidal illumination to measure the 3d shape of translucent objects, *Proc. of IEEE Conference on Computer Vision and Pattern Recognition* (2011).

[7] Chen, T., Lensch, H. P. A., Fuchs, C. and Seidel, H. P.: Polarization and Phase-shifting for 3d Scanning of Translucent Objects, *Proc. of IEEE Conference on Computer Vision and Pattern Recognition* (2007).

[8] Goesele, M., Lensch, H. P. A., Lang, J., Fuchs, C. and Seidel, H. P.: DISCO - Acquisition of Translucent Objects, *Proc. of ACM SIGGRAPH*, pp. 835–844 (2004).

[9] Nayar, S. K., Krishnan, G., Grossberg, M. D. and Raskar, R.: Fast Separation of Direct and Global Components of a Scene using High Frequency Illumination, *Proc. of ACM SIGGRAPH*, Vol. 25, pp. 935–944 (2006).

[10] Tanaka, K., Mukaigawa, Y., Matsushita, Y. and Yagi, Y.: Descattering of transmissive observation using Parallel High-Frequency Illumination, *Proc. of IEEE International Conference on Computational Photography* (2013).

[11] Reddy, D., Ramamoorthi, R. and Curless, B.: Frequency-space decomposition and acquisition of light transport under spatially varying illumination, *Proc. of European Conference on Computer Vision* (2012).

[12] Gupta, M., Agrawal, A., Veeraraghavan, A. and Narasimhan, S. G.: A Practical Approach to 3D Scanning in the Presence of Interreflections, Subsurface Scattering and Defocus, *International Journal of Computer Vision*, Vol. 102, pp. 33–55 (2013).

[13] Chen, T., Seidel, H.-P. and Lensch, H. P. A.: Modulated phase-shifting for 3D scanning, *Proc. of IEEE Conference on Computer Vision and Pattern Recognition* (2008).

[14] Mukaigawa, Y., Yagi, Y. and Raskar, R.: Analysis of Light Transport in Scattering Media, *Proc. of IEEE Conference on Computer Vision and Pattern Recognition* (2010).

[15] Narasimhan, S. G., Gupta, M., Donner, C., Ramamoorthi, R., Nayar, S. K. and Jensen, H. W.: Acquiring scattering properties of participating media by dilution, *Proc. of ACM SIGGRAPH*, pp. 1003–1012 (2006).

[16] Hawkins, T., Einarsson, P. and Debevec, P.: Acquisition of time-varying participating media, *ACM Trans. on Graph.*, Vol. 24, No. 3, pp. 812–815 (2005).

[17] Jensen, H. W., Marschner, S. R., Levoy, M. and Hanrahan, P.: A Practical Model for Subsurface Light Transport, *Proc. of ACM SIGGRAPH* (2001).

[18] Mukaigawa, Y., Suzuki, K. and Yagi, Y.: Analysis of Subsurface Scattering based on Dipole Approximation, *IP SJ Transactions on Computer Vision and Applications*, Vol. 1, pp. 128–138 (2009).

[19] Gkioulekas, I., Xiao, B., Zhao, S., Adelson, E. H., Zickler, T. and Bala, K.: Understanding the Role of Phase Function in Translucent Appearance, *ACM Trans. on Graph.*, Vol. 32, No. 5, p. 147 (2013).

[20] Velten, A., Wu, D., Jarabo, A., Masia, B., Barsi, C., Joshi, C., Lawson, E., Bawendi, M., Gutierrez, D. and Raskar, R.: Femto-photography: Capturing and visualizing the propagation of light, *ACM Trans. on Graph.*, Vol. 32, No. 4, p. 44 (2013).

[21] Wu, D., O Toole, M., Velten, A., Agrawal, A. and Raskar, R.: Decomposing Global Light Transport using Time of Flight Imaging, *Proc. of IEEE Conference on Computer Vision and Pattern Recognition* (2013).

[22] Wu, D., Wetzstein, G., Barsi, C., Willwacher, T., Dai, Q. and Raskar, R.: Ultra-fast Lensless Computational Imaging through 5D Frequency Analysis of Time-resolved Light Transport, *International Journal of Computer Vision*, Vol. 110, No. 2, pp. 128–140 (2014).

[23] Horn, B. K. P.: Shape from shading: A method for obtaining the shape of a smooth opaque object from one view, Technical report, Massachusetts Institute of Technology (1970).

[24] Woodham, R. J.: Photometric method for determining surface orientation from multiple images, *Optical Engineering*, Vol. 19, No. 1, pp. 139–144 (1980).

[25] Sankaranarayanan, A. C., Veeraraghavan, A., Tuzel, O. and Agrawal, A.: Specular surface reconstruction from sparse reflection correspondences, *Proc. of IEEE Conference on Computer Vision and Pattern Recognition* (2010).

[26] Kobayashi, Y., Morimoto, T., Sato, I., Mukaigawa, Y. and Ikeuchi, K.: Reconstructing Shape and Appearance of Thin Film Objects with Hyper Spectral Sensor, *Proc. of Asian Conference on Computer Vision* (2014).

[27] Liao, M., Wang, L., Yang, R. and Gong, M.: Light fall-off stereo, *Proc. of IEEE Conference on Computer Vision and Pattern Recognition* (2007).

[28] Huynh, C. P., Robles-Kelly, A. and Hancock, E.: Shape and refractive index recovery from single-view polarisation images, *Proc. of IEEE Conference on Computer Vision and Pattern Recognition* (2010).

[29] Nayar, S. K., Ikeuchi, K. and Kanade, T.: Shape from interreflections, *International Journal of Computer Vision*, Vol. 6, pp. 173–195 (1991).

[30] Liu, S., Ng, T.-T. and Matsushita, Y.: Shape from Second-bounce of Light Transport, *Proc. of European Conference on Computer Vision* (2010).

[31] Ding, Y., Li, F., Ji, Y. and Yu, J.: Dynamic Fluid Surface Acquisition Using a Camera Array, *Proc. of International Conference on Computer Vision* (2011).

[32] Wetzstein, G., Roodnick, D., Heidrich, W. and Raskar, R.: Refractive shape from light field distortion, *Proc. of International Conference on Computer Vision* (2011).

[33] Morris, N. J. and Kutulakos, K. N.: Reconstructing the surface of inhomogeneous transparent scenes by scatter trace photography, *Proc. of International Conference on Computer Vision* (2007).

[34] Ma, C., Lin, X., Suo, J., Dai, Q. and Wetzstein, G.: Transparent Object Reconstruction via Coded Transport of Intensity, *Proc. of IEEE Conference on Computer Vision and Pattern Recognition*, pp. 3238–3245 (2014).

[35] Narasimhan, S. G., Nayar, S. K., Sun, B. and Koppal, S. J.: Struc-

- tered light in scattering media, *Proc. of International Conference on Computer Vision* (2005).
- [36] Tsiotsios, C., Angelopoulou, M. E., Kim, T.-K. and Davison, A. J.: Backscatter Compensated Photometric Stereo with 3 Sources, *Proc. of IEEE Conference on Computer Vision and Pattern Recognition* (2014).
- [37] Dong, B., Moore, K. D., Zhang, W. and Peers, P.: Scattering Parameters and Surface Normals from Homogeneous Translucent Materials using Photometric Stereo, *Proc. of IEEE Conference on Computer Vision and Pattern Recognition* (2014).
- [38] Hecht, E.: *Optics*, Addison-Wesley (2002).
- [39] Lambert, J. H.: *Photometria sive de mensura de gratibus luminis*, Eberhard Klett In Eberhard Klett (1760).
- [40] of Standards, U. S. N. B. and Nicodemus, F. E.: *Geometrical considerations and nomenclature for reflectance*, Vol. 160, US Department of Commerce, National Bureau of Standards Washington, D. C (1977).
- [41] Donner, C., Lawrence, J., Ramamoorthi, R., Hachisuka, T., Jensen, H. W. and Nayar, S. K.: An Empirical BSSRDF Model, *Proc. of ACM SIGGRAPH* (2009).
- [42] Levoy, M., Chen, B., Vaish, V., Horowitz, M., McDowall, I. and Bolas, M.: Synthetic Aperture Confocal Imaging, *Proc. of ACM SIGGRAPH*, pp. 825–834 (2004).
- [43] Tagawa, S., Mukaigawa, Y., Kim, J., Raskar, R., Matsushita, Y. and Yagi, Y.: Hemispherical Confocal Imaging, *IP SJ Trans. on Computer Vision and Applications*, Vol. 3, pp. 222–235 (2011).
- [44] Nayar, S. K., Fang, X.-S. and Boulton, T.: Separation of Reflection Components Using Color and Polarization, *International Journal of Computer Vision*, Vol. 21, pp. 163–186 (1997).
- [45] Nishino, K., Zhang, Z. and Ikeuchi, K.: Determining Reflectance Parameters and Illumination Distribution from a Sparse Set of Images for View-dependent Image Synthesis, *Proc. ICCV2001* (2001).
- [46] Beer, A.: Bestimmung der Absorption des rothen Lichts in farbigen Flussigkeiten, *Annalen der Physik und Chemie*, Vol. 86, pp. 78–88 (1852).
- [47] Henyey, L. G. and Greenstein, J. L.: Diffuse radiation in the galaxy, *Astrophysical Journal*, Vol. 93, pp. 70–83 (1941).
- [48] Kennedy, J. and Eberhart, R. C.: Particle swarm optimization, *IEEE International Conference on Neural Networks* (1995).
- [49] Nelder, J. A. and Mead, R.: A Simplex Method for Function Minimization, *The Computer Journal*, Vol. 7, pp. 308–313 (1965).
- [50] Ikehata, S., Wipf, D., Matsushita, Y. and Aizawa, K.: Robust Photometric Stereo using Sparse Regression, *Proc. of IEEE Conference on Computer Vision and Pattern Recognition* (2012).
- [51] Wu, L., Ganesh, A., Shi, B., Matsushita, Y., Wang, Y. and Ma, Y.: Robust Photometric Stereo via Low-Rank Matrix Completion and Recovery, *Proc. of Asian Conference on Computer Vision* (2010).
- [52] Moore, K. D. and Peers, P.: An empirical study on the effects of translucency on photometric stereo, *The Visual Computer*, Vol. 29, No. 6-8, pp. 817–824 (2013).
- [53] Munoz, A., Echevarria, J. I., Seron, F. J., Lopez-Moreno, J., Glen-cross, M. and Gutierrez, D.: BSSRDF Estimation from Single Images, *Computer Graphics Forum*, Vol. 30, No. 2, pp. 455–464 (2011).
- [54] Dong, B., Moore, K., Zhang, W. and Peers, P.: Scattering Parameters and Surface Normals from Homogeneous Translucent Materials using Photometric Stereo, *Proc. of IEEE Conference on Computer Vision and Pattern Recognition* (2014).
- [55] Munoz, A., Echevarria, J. I., Seron, F. J. and Gutierrez, D.: Convolution-Based Simulation of Homogeneous Subsurface Scattering, *Computer Graphics Forum*, Vol. 30, No. 8, pp. 2279–2287 (2011).
- [56] d'Eon, E. and Irving, G.: A quantized-diffusion model for rendering translucent materials, *ACM Transactions on Graphics (TOG)*, Vol. 30 (2011).
- [57] Kim, T. H., Ahn, B. and Lee, K. M.: Dynamic Scene Deblurring, *Proc. of International Conference on Computer Vision*, IEEE, pp. 3160–3167 (2013).
- [58] Kim, T. H. and Lee, K. M.: Segmentation-Free Dynamic Scene Deblurring, *Proc. of IEEE Conference on Computer Vision and Pattern Recognition*, pp. 2766–2773 (2014).
- [59] Agrawal, A., Raskar, R. and Chellappa, R.: What Is the Range of Surface Reconstructions from a Gradient Field?, *Proc. of European Conference on Computer Vision* (2006).
- [60] Gu, J., Kobayashi, T., Gupta, M. and Nayar, S. K.: Multiplexed illumination for scene recovery in the presence of global illumination, *Proc. of International Conference on Computer Vision* (2011).
- [61] Gao, L., Liang, J., Li, C. and Wang, L. V.: Single-shot compressed ultrafast photography at one hundred billion frames per second, *Nature*, Vol. 16, No. 7529, pp. 74 – 77 (2014).